JOURNAL OF PROPULSION AND POWER
Vol. 26, No. 2, March–April 2010

Modeling of Fixed-Exit Porous Bleed Systems for Supersonic Inlets

John W. Slater* and John D. Saunders†
NASA John H. Glenn Research Center at Lewis Field, Cleveland, Ohio 44135

DOI: 10.2514/1.37390

A model has been developed to simulate porous bleed systems with fixed-area plenum exits in supersonic inlets. The fixed-exit bleed model computes the bleed plenum static pressure and bleed rates according to local flow conditions and the fixed-exit characteristics of the bleed system. The model was implemented into the Wind-US computational fluid dynamics code. The behavior of the model was demonstrated through computational fluid dynamics simulations of the flow through a Mach 3.0 axisymmetric, mixed-compression inlet. The model was able to capture the variation of bleed rates across a bleed region, especially variations due to shocks interacting with the bleed region. The model was able to accurately indicate the characteristic cane curves showing the variation of the engine-face total pressure recovery with respect to the total bleed rate or the engine-face flow ratio, which varied with the level of inlet backpressure. The fixed-exit model provided a more realistic simulation of the onset of inlet unstart than the existing bleed model, which assumed constant plenum pressures. The fixed-exit bleed model was less accurate in determining plenum pressures and indicated higher plenum pressures than observed in the inlet wind-tunnel test. The results highlight aspects of porous bleed models that require further research.

Nomenclature

A	=	area
D	=	bleed hole diameter
L	=	bleed hole length
M	=	Mach number
p	=	pressure
p_{t0}	=	tunnel reference total pressure (15.0 psi)
R	=	gas constant
r	=	radius
r_c	=	cowl lip radius (10.0 in.)
T	=	temperature
W	=	rate of flow
γ	=	ratio of specific heats
δ	=	boundary-layer thickness
ρ	=	density

Subscripts

B	=	property evaluated at a boundary point
exit	=	property evaluated at the bleed plenum exit
plenum	=	averaged property evaluated in the plenum
t	=	total condition
δ	=	property evaluated at the boundary-layer edge
0	=	reference conditions ahead of the inlet
2	=	averaged engine-face conditions

I. Introduction

EFFICIENT supersonic flight requires an efficient system for the compression and deceleration of the flow of air through the inlet for the generation of thrust by the propulsion system [1,2]. The inlet compresses the flow by establishing a system of oblique shock waves externally and internally to the inlet. A normal terminal shock within the internal throat of the inlet decelerates the flow from supersonic to subsonic speeds for intake by the gas turbine engine. The interactions of the shocks with turbulent boundary layers on the surfaces of the inlet can degrade the boundary layer and lead to boundary-layer separation, which decreases inlet performance [3–6]. Significant separation may result in instability in the propulsion system, which may manifest itself as an inlet unstart in which the internal shock system is expelled from the inlet. Inlet unstart is a severe event for an aircraft and should be avoided.

One option for alleviating the adverse effects of shock/boundary-layer interactions is the placement of porous bleed regions on the inlet surfaces in the vicinity of the interactions [1–7]. Porous bleed consists of perforations in the surfaces through which a small fraction of the inlet flow is extracted. The extracted flow is mostly the lower-momentum portion of the boundary layer. This leaves the remaining boundary layer with a higher average momentum, which improves its ability to negotiate the adverse pressure gradient associated with shock/boundary-layer interactions. A secondary function of bleed is to help stabilize the terminal shock within the inlet throat [8,9]. The terminal shock is pushed upstream by an increase in the static pressure at the engine face due to a decrease in the engine-flow rate. As the terminal shock moves upstream into the bleed regions in the throat, the bleed flow increases to compensate up for the decrease of flow to the engine face and thereby inhibits the upstream motion of the shock.

The perforations of the porous bleed regions are commonly circular holes with a diameter much smaller than the inlet scales (e.g., inlet length or cross-sectional diameter) [1–3,7]. The bleed holes are usually located on the surfaces in bands or groups of rows and the number of bleed holes can be in the hundreds. The bleed system extracts flow into a plenum that has a static pressure lower than the local inlet flow. The rate of bleed flow increases as the plenum pressure decreases; however, the flow through the bleed holes will eventually choke and the flow rate will reach a maximum [3]. The plenum is usually sized large enough to allow the speed of the bleed flow to decrease and static pressures throughout the plenum to equalize. The bleed flow leaves the plenum through ducting and an exit. Although some of the bleed flow could be used by the propulsion system or another system in the aircraft, a common approach is to dump the bleed flow overboard to the external flow. This adds a component of drag termed bleed drag that accounts for the loss of momentum of the dumped flow [1,2]. The exit is usually

Presented as Paper 94 at the 46th AIAA Aerospace Sciences Meeting and Exhibit, Reno, NV, 7–10 January 2008; received 3 March 2008; revision received 25 October 2009; accepted for publication 23 November 2009.

*Aerospace Engineer, Inlet and Nozzle Branch, Mail Stop 5–12, 21000 Brookpark Road. Senior Member AIAA.

†Aerospace Engineer, Inlet and Nozzle Branch, Mail Stop 5–12, 21000 Brookpark Road.

designed to dump the flow supersonically and approximately in line with the external flow or at a location, which might reduce base drag [2,3]. Dumping the flow supersonically ensures that the external pressure waves do not enter the plenum via the exit and affect the plenum static pressure. The ducting between the plenum and exit can be significant. For example, a bleed plenum for a bleed region on the centerbody of an axisymmetric inlet may have a duct that is directed through the centerbody and then through a support strut to reach the exit located on the external surface of the cowl [2,7,9].

The operation of the bleed system requires that the plenum pressure be maintained at lower static pressures than the local inlet flow. The lower pressure is obtained from the external flow via the ducting and exit [2,3,7]. The exit operates as a converging–diverging nozzle with choked flow at the throat so that the flow is dumped supersonically. Thus, the size of the exit area controls the plenum pressure and so the bleed rate. Some bleed systems are designed such that the plenum static pressure is at such a low level as to cause the flow through the bleed holes to be choked; however, this can lead to increased levels of bleed drag, particularly for the bleed regions in the throat [2,3]. The alternative is to maintain a higher plenum pressure so that the bleed holes are not choked, but that the bleed system is still effective in extracting the desired bleed flow [7–9].

It is possible to have a control system that adjusts the size of the exit area and so controls the plenum pressure [8,9]. This can be done mechanically or by fluidic means. The stability of the inlet against inlet unstart can be improved by controlling the plenum pressure to maintain a near-constant plenum pressure as the terminal shock encounters the throat bleed regions and the bleed rate increases [8]. The increased bleed rate delays the forward motion of the terminal shock. At some point, the bleed system can no longer contain the terminal shock and the terminal shock goes forward of the throat bleed regions and the onset of inlet unstart has occurred.

A control system adds complexity and weight to the bleed system. For a low-cost or expendable vehicle, a control system may not be desired. In such a case, a fixed-exit area may be sufficient to extract the desired bleed flow over the range of operations of the inlet. This is termed a fixed-exit bleed system. Although a fixed-exit bleed system is simpler, it will likely result in lower margin of stability than a controlled, constant-pressure system.

The analysis of supersonic inlet flows with porous bleed systems has been demonstrated using methods of computational fluid dynamics (CFD) [10–15]. The simulation of the bleed regions and their effect on the flow is a critical aspect of such analysis. It is possible to directly simulate the flow through the bleed holes and plenum and several CFD studies have demonstrated these type of simulations [16–19]. The CFD simulations show that the flow through an individual bleed hole can be complex. The turning of the flow into the hole can result in a recirculation region within the hole with formation of significant shear layers. Shock waves can form within the bleed hole. The flow may be accelerated to create a supersonic jet that may extend into the plenum. The complexity of the flow in a bleed hole, the small scale of the porous bleed holes, and the sheer number of bleed holes in an inlet has led to the development of global bleed boundary condition models that capture the overall effect of the bleed region on the inlet flow rather than resolving the flow through each bleed hole [13,20–26]. The model of Mayer and Paynter [13] is one bleed model that was implemented into the Wind-US CFD code [27] and represents the current state of porous bleed modeling in a production CFD flow solver. The supersonic inlet analyses of [15] demonstrated the use of this bleed model. The Mayer–Paynter model allows the bleed rate to vary across the bleed region according to local conditions. The Mayer–Paynter model assumes that the bleed plenum static pressure is controlled to remain at a constant, specified value: a constant-pressure bleed model.

This paper discusses the modification of the Mayer–Paynter bleed model to impose the condition of a fixed-exit area bleed plenum. The next section describes the details of the bleed modeling and its implementation into the Wind-US CFD flow solver. The operation of the constant-pressure and fixed-exit bleed models is demonstrated through the CFD simulation of flow through a Mach 3.0 axisymmetric, mixed-compression supersonic inlet. The results of the CFD simulations are compared to wind-tunnel data for the inlet performance, surface static pressures, bleed rates, and bleed plenum pressures.

II. Porous Bleed System Modeling

The modeling of a porous bleed system with a fixed-exit plenum is described in this section. The model is then formulated as a boundary condition for Wind-US CFD code.

A. Description of a Porous Bleed System with a Fixed-Exit Plenum

A schematic of a porous bleed system with a fixed-exit plenum is shown in Fig. 1. The schematic is representative of a bleed system located in the cowl of a supersonic inlet [7–9,28]. The core inlet flow is shown at the bottom of the figure with a boundary layer formed on the surface of the inlet. The boundary-layer thickness at a point along the surface is indicated as δ. The Mach number, total pressure, and total temperature at the edge of the boundary layer are indicated as M_δ, $p_{t\delta}$, and $T_{t\delta}$, respectively. These values can and do change over the length of the bleed region, especially if a shock is interacting within the bleed region.

The inlet surface has a porous bleed region containing numerous bleed holes. The bleed region extends over an area of A_{region} on the inlet surface. An amount of flow W_{holes} is extracted from the core inlet flow and drawn through the bleed holes into the plenum when the plenum static pressure p_{plenum} is lower than the local static pressure in the core inlet flow.

A normal shock is shown interacting with the boundary layer and bleed region. The normal shock extends into the boundary layer to the sonic line. The local flow may cause the shock to bend and/or bifurcate as it interacts with the boundary layer. The schematic shows an attached boundary layer in which its thickness is decreasing downstream of the shock due to the action of the bleed. Although this is a desirable objective, the actual change in boundary-layer thickness depends on the boundary-layer profile approaching the bleed region, the local bleed rate, and the strength of the shock/boundary-layer interaction. Boundary-layer separation could occur if the approaching boundary layer was severely distorted, shock was stronger, or bleed rates were lower.

The arrows show the relative amount of flow through each bleed hole. The bleed flow is greater downstream of the shock due to the increase in the local static pressure across the normal shock. The flow rate through the bleed holes can reach a maximum when the plenum static pressure is below a critical value. The bleed holes are considered choked. The flow through a bleed hole forms a jet that is injects the flow into the plenum. This jet can accelerate to supersonic speeds for low enough plenum pressures and can maintain its structure for several hole diameters into the plenum. For the model, we assume the plenum is of large enough volume such that the flow through the holes is dissipated and the average flow velocity reaches low subsonic values or $M_{\text{plenum}} \approx 0$. Thus, the plenum total pressure $p_{t\text{plenum}}$ is approximated as equivalent to the plenum static pressure p_{plenum}.

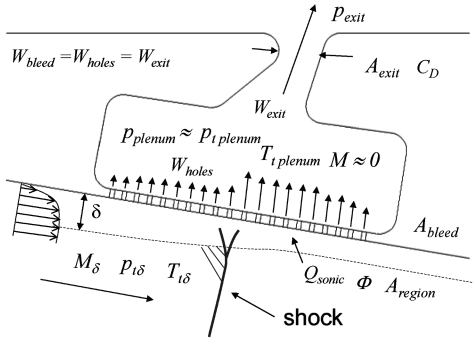

Fig. 1 Schematic of a fixed-exit bleed system.

The bleed flow exits the plenum through a duct and exit. The amount of flow exiting through the plenum exit is represented as W_{exit}. The schematic shows a short, simple exit duct characterized by an exit area A_{exit}, which is the minimum cross-sectional area that the flow encounters as it exits the plenum. The losses of the flow through the exit duct and exit are characterized by a discharge coefficient C_D. The static pressure of the exit p_{exit} is assumed to occur at the location of A_{exit} and for the schematic shown would be approximately equal to or greater than the static pressure of the exterior flow. The bleed system is usually operated such that the exit flow is choked at the exit-area location. This ensures that the external flow pressure does not affect the bleed plenum or influence the bleed plenum condition through the transmission of pressure waves.

B. Porous Bleed Region Modeling

The flow through the porous bleed region is modeled by first assuming the region is continuously porous. The porosity Φ of the region is defined as

$$\Phi = \frac{A_{\text{bleed}}}{A_{\text{region}}} \tag{1}$$

where A_{bleed} is the sum of the cross-sectional areas of all the bleed hole openings in the region. Individual holes are not resolved or recognized and the local bleed flow can be calculated at any point on the bleed region.

The local bleed flow through the bleed holes is calculated in the form of

$$W_{\text{holes}} = Q_{\text{sonic}}\ W_{\text{sonic}} \tag{2}$$

The W is the flow rate expressed in terms of total pressure, total temperature, and Mach number in the form of

$$W = p_t A M \left(\frac{\gamma}{RT_t}\right)^{1/2} \left(1 + \frac{\gamma - 1}{2} M^2\right)^{-(\gamma+1)/2(\gamma-1)} \tag{3}$$

The W_{sonic} is a reference sonic flow rate defined as

$$W_{\text{sonic}} = p_{t\delta} \Phi A_{\text{region}} \left(\frac{\gamma}{RT_{t\delta}}\right)^{1/2} \left(\frac{\gamma + 1}{2}\right)^{-(\gamma+1)/2(\gamma-1)} \tag{4}$$

The Mach number is assumed to be sonic ($M = 1$) and the values of total pressure and total temperature are those at the edge of the boundary layer ($p_{t\delta}, T_{t\delta}$). One can regard W_{sonic} as the flow rate obtained by assuming sonic, isentropic flow through the bleed holes.

The Q_{sonic} is the sonic flow coefficient and was evaluated based on empirical data [3,13,29,30]. The sonic flow coefficient is dependent on the flow approaching the bleed region and on the geometric properties of the bleed hole, such as the hole angle, hole diameter, and shape of the hole cross section. The work of McLafferty and Ranard has been a common source of sonic flow coefficient data [29]. Willis, Davis, and Hingst provided a study on how the sonic flow coefficient varied with various supersonic Mach numbers and geometric factors [30]. The approach for collecting the sonic flow coefficient data involved wind-tunnel experiments of uniform flow over a flat plate containing a porous bleed region. For a certain plenum pressure, the bleed flow rate was measured. Equations (2) and (4) were used to calculate Q_{sonic}. The variation of Q_{sonic} with respect to the plenum pressure ratio was obtained by varying the plenum pressure from values that produced near zero bleed flow to values that produced the maximum bleed flow. The variation of Q_{sonic} was correlated to the Mach number at the edge of the approaching boundary layer M_δ and the bleed plenum pressure ratio defined as

$$\text{Bleed plenum pressure ratio} = \frac{p_{\text{plenum}}}{p_{t\delta}} \tag{5}$$

Figure 2 shows the data for the sonic flow coefficient that is used within the Wind-US CFD code. It is based on a combination of data from [3] and Boeing internal data [13] for circular bleed holes at 90 deg angles to the surface with a length-to-diameter ratio of $L/D = 3$. The Mayer–Paynter bleed model used a table look up of the data presented in Fig. 2. Each curve corresponds to a specific approach Mach number. At the right end of the curve, the sonic flow coefficient is zero, which indicates a zero bleed rate. As the plenum pressure ratio is reduced, a greater amount of bleed is extracted and the sonic flow coefficient increases. At some critical plenum pressure ratio, the maximum rate of flow through the bleed holes is reached and the sonic flow coefficient no longer increases as the plenum pressure ratio is further reduced. The flow through the bleed holes becomes choked.

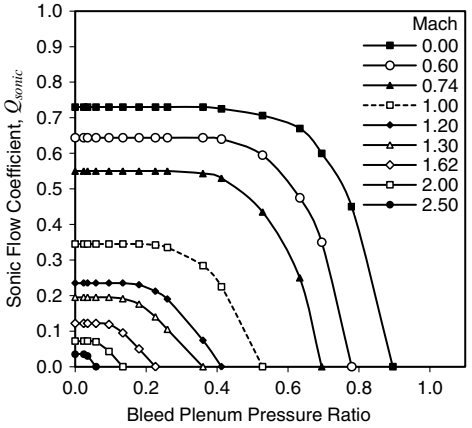

Fig. 2 Sonic flow coefficient data for 90 deg bleed holes.

C. Modeling of the Flow Through the Plenum Exit

The rate of flow through the plenum exit W_{exit} is modeled as

$$W_{\text{exit}} = C_D W_{\text{ideal}} \tag{6}$$

where the ideal flow rate through the plenum exit is

$$W_{\text{ideal}} = p_{\text{plenum}} A_{\text{exit}} M_{\text{exit}} \left(\frac{\gamma}{RT_{\text{plenum}}}\right)^{1/2} \times \left(1 + \frac{\gamma - 1}{2} M_{\text{exit}}^2\right)^{-(\gamma+1)/2(\gamma-1)} \tag{7}$$

The calculation of the ideal flow rate assumes isentropic flow through the exit duct with the total conditions of those of the plenum. Because the average Mach number in the bleed plenum is assumed to be very small, the total pressure and total temperature of the plenum are approximately equal to the static pressure and static temperature, respectively. The A_{exit} is the cross-sectional area at the exit.

The Mach number at the bleed plenum exit M_{exit} depends on the ratio of the static pressure at the plenum exit p_{exit} to the static pressure of the plenum. If $p_{\text{exit}}/p_{\text{plenum}} < 0.528$, then the flow through the bleed plenum exit is choked and Eq. (7) is evaluated with $M_{\text{exit}} = 1$. If $p_{\text{exit}}/p_{\text{plenum}} > 0.528$, then the flow through the bleed plenum exit is subsonic. For isentropic, subsonic flow through the bleed exit, M_{exit} can be calculated from the definition of total pressure with the value of total pressure equal to the plenum pressure and the static pressure equal to the exit static pressure.

The discharge coefficient C_D represents the reduction in the flow rate because of irreversibility and losses in the flow through the exit. The value of C_D is seldom known without wind-tunnel data and is not usually presented in inlet performance literature. It can be estimated by solving Eqs. (6) and (7) using a known flow rate, exit area, and plenum conditions.

D. Fixed-Exit Modeling

Modeling the flow through a porous bleed system with a fixed-exit area is based on the balance of flow between what enters in through the porous bleed holes W_{holes} and what exits through the plenum exit W_{exit}, or

$$W_{\text{bleed}} = W_{\text{holes}} = W_{\text{exit}} \tag{8}$$

The bleed plenum static pressure p_{plenum} controls the flow through the bleed holes W_{holes} and the flow through the bleed plenum exit W_{exit}. Figure 3 illustrates how both flows vary with respect to p_{plenum}. Equation (2) defines the behavior of W_{holes} with respect to p_{plenum}. If the p_{plenum} is equal to the local static pressure at the surface of the inlet, then $W_{\text{holes}} = 0$. This point is labeled point A in Fig. 3. As p_{plenum} decreases, W_{holes} increases. Eventually, the flow through the bleed holes chokes and the W_{holes} reach a maximum flow rate. Equation (6) defines the variation of W_{exit} with respect to p_{plenum} and that variation is also plotted in Fig. 3. If the $p_{\text{plenum}} = p_{\text{exit}}$, then $W_{\text{exit}} = 0$. This point is labeled point B in Fig. 3. As p_{plenum} increases, the flow through the exit is subsonic and increases until the flow becomes choked through the exit. As p_{plenum} increases further, W_{exit} increases linearly per Eq. (7) with $M_{\text{exit}} = 1$. The flow balance of Eq. (8) indicates that the bleed system will operate at the p_{plenum} at which the two curves described above intersect, as shown in Fig. 3 as point C. Thus, the fixed-exit bleed model involves an iteration to find the plenum pressure that solves Eq. (8) and yields the intersection of Eqs. (2) and (6).

E. Bleed Boundary Condition

Within a CFD code, the bleed model is imposed as a boundary condition for those surface grid points contained within a bleed region. The effect of the bleed model is to set the normal velocity component in the manner of

$$v_N = \frac{W_{\text{holes}}}{\rho_B A_B} \tag{9}$$

at each of the surface grid points within the bleed region. The A_B is the boundary cell surface area associated with the surface grid point and it replaces A_{region} in the evaluation of Eq. (4) for the boundary grid point. The Mach number M_δ, total pressure $p_{t\delta}$, total temperature $T_{t\delta}$ are evaluated at the edge of the boundary layer. The location of the edge of the boundary layer is specified by selecting a solution grid point above the surface grid point estimated to be at the edge of the boundary layer. The flow conditions are then evaluated at that solution point. The solution grid point at the edge of the boundary layer is specified as a number of grid points away from the wall for each bleed region. The value of Q_{sonic} required for Eq. (2) is evaluated using the table lookup of the data of Fig. 2 using the boundary-layer edge conditions. The total temperature in the plenum T_{plenum} required for Eq. (7) is assumed to be equal to the total temperature at the edge of the boundary layer based on an assumption of adiabatic flow.

The normal component of velocity evaluated by Eq. (9) is then combined with the tangential component of velocity as determined by the slip or no-slip wall boundary condition. It is recognized that the bleed can induce a tangential component of velocity in addition to the normal component; however, the bleed model assumes this quantity is small enough to be ignored. This is certainly a topic for further research. The bleed model also does not allow the normal velocity component to be directed into the inlet core flow, which would involve injection of flow from the bleed plenum into the core flow. This reverse bleed or blowing is physically possible if the plenum pressure is greater than the local static pressure.

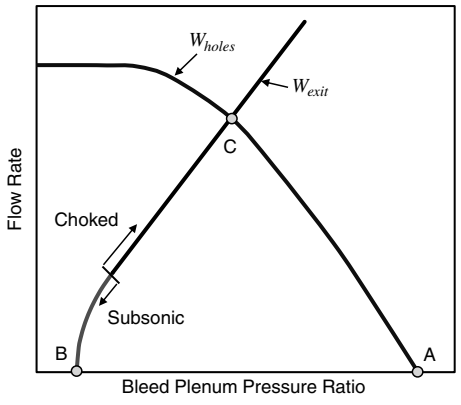

Fig. 3 Flow through the bleed holes and the bleed plenum exit.

An implied assumption of the bleed model is that the Q_{sonic} empirical data of Fig. 2 can be applied for flowfields other than uniform flow over a flat plate and for bleed holes with $L/D \neq 3.0$. Harloff and Smith [22] suggest that for bleed holes with $L/D < 3$, there are small differences in the bleed flow. A real inlet flow will contain shock waves, adverse pressure gradients, and perhaps severe boundary layers distorted to the point of separation. The bleed boundary condition will evaluate Q_{sonic} for the local conditions it finds at the estimated edge of the boundary layer. The edge of the boundary layer itself may not be well defined, such as would be the case for a shock/boundary-layer interaction with separation. Further, the estimated edge of the boundary layer may lie across an oblique shock and not represent conditions at the surface of the bleed region. Such concerns led to a few alternatives for calculating the properties at the edge of the boundary layer. The approach that provided the most realistic bleed for shock/boundary-layer interactions was to evaluate $p_{t\delta}$ using the static pressure at the surface grid point and M_δ. A better approach would be to correlate Q_{sonic} with surface properties at the bleed region rather than properties at the edge of the boundary layer.

F. Implementation into the Wind-US CFD Code

The fixed-exit bleed model was implemented into the Wind-US CFD code [27], which was then used to perform the simulations of this paper. Wind-US solves the Reynolds-averaged Navier–Stokes (RANS) equations for turbulent, compressible flows using a cell-vertex, finite volume, time-marching approach. The cell-face fluxes are computed using an upwind-biased formulation. Steady flows are solved in a time-dependent manner using a first-order, Euler implicit method with local time stepping.

III. CFD Simulations of the NASA 1507 Inlet

The bleed models were demonstrated through CFD simulations for the flow through the NASA 1507 supersonic inlet [28]. It is referred to here as the NASA 1507 inlet after its report number, NASA Technical Memorandum X-1507. The inlet was chosen for this study because of its simple, axisymmetric shape and because it contained porous bleed regions with plenums with fixed-exit areas. In addition, the available wind-tunnel data allowed evaluation of the bleed model for determining bleed flow rates, bleed plenum pressures, and inlet performance. The sections below describe the inlet and CFD simulations and compares the CFD results with the wind-tunnel data.

A. Inlet Description

The NASA 1507 inlet was designed for Mach 3.0 and used an axisymmetric centerbody and cowl. The tunnel conditions used for the CFD simulations were a Mach number of 3.0, Reynolds number of 2.0×10^6 per foot, total pressure of $p_{t0} = 15.0$ psia, and zero angle of attack. The centerbody had a conical half-angle of 12.5 deg that compressed the flow externally through a conical shock and through the turning of the flow outward in the radial direction. The sharp-lipped, circular cowl captured the flow and directed the flow into the inlet duct. The flow was compressed and turned internally through a series of oblique shock waves and internal area contraction. Localized compressions and expansions turned the flow back toward the axis of the inlet. A normal terminal shock located within the throat decelerated the flow to subsonic speeds. The subsonic diffuser further decelerated and compressed the flow for delivery to the engine face. Of the two subsonic diffusers tested, the CFD simulations modeled the shorter subsonic duct of length $3.0r_c$. Vortex generators were located along the circumference of the subsonic diffuser on both the centerbody and cowl; however, these were not modeled in the CFD simulations. Four equally spaced support struts connected the center body and cowl and were located downstream of

the engine-face rake location. These were not modeled in the CFD simulations.

The inlet contained four porous bleed regions: two on the centerbody and two on the cowl. Table 1 presents the locations and properties of the bleed regions. The forward two bleed regions (I and II) helped control the boundary layer through its interactions with the oblique shock waves. The aft two bleed regions (III and IV) were in the throat and served to control the interaction of the terminal shock with the boundary layers, as well as provide some control of the forward movement of the terminal shock. The bleed holes were circular and at angles of 90 deg to the inlet surface. Bleed regions I and II consisted of several rows of bleed holes and Table 1 lists the start and end axial locations of the hole centers for the first and last rows, respectively. The axial locations are normalized by the cowl lip radius x/r_c. Bleed region III was located on the cowl and consisted of two rows of bleed holes. Bleed region IV consisted of five rows of bleed holes on the centerbody. Table 1 lists the axial location of the centers of the rows for bleed regions III and IV. The length-to-diameter ratios L/D of the bleed holes vary between 0.5 and 2.5 and are listed in Table 1. It is assumed that the empirical data for Q_{sonic} of Fig. 2 sufficiently represents the bleed flow through the bleed holes of this inlet. Each compartmented bleed region fed into its own plenum with separate ducting and exits. The plenum exits had fixed areas.

The values of the bleed plenum exit areas A_{exit} and discharge coefficients C_D for each bleed region were not listed in [28]. The approach for obtaining values of C_D and A_{exit} required for Eqs. (6) and (7), respectively, involved solving the combination of Eqs. (6–8) for the product $C_D A_{\text{exit}}$ for each bleed region using the bleed rates, plenum pressures, and plenum temperatures known from the supercritical condition. In addition, all plenum exits were assumed to be choked ($M_{\text{exit}} = 1$), which should be the case for Mach 3.0 external flow with a very low external pressure. At the supercritical condition, the terminal shock is downstream of the throat bleed regions III and IV. Table 2 summarizes the supercritical bleed rates from the experiment. The values correspond to bleed exit setting B from [28]. The bleed rates are normalized by the reference capture flow rate W_C, which is calculated using the frontal area of the cowl lip ($A_C = \pi r_c^2$) and the reference conditions ahead of the inlet. The plenum pressures are normalized by the reference total pressure p_{t0}. The bleed rates and plenum pressures obtained in the CFD simulation for the supercritical condition are listed in Table 2. In the CFD simulations, the plenum pressures were adjusted until the bleed rate for each bleed region matched closely to that of the experiment. The resulting plenum pressure for bleed region I from the simulation matched well with the experiment; however, the pressures for bleed regions II, III, and IV were significantly higher. The reasons for why they are higher could be related to uncertainties in the location of the measurements in the experiment.

Table 1 Location and properties of the bleed regions.

x/r_c	D, in	Φ	L/D
Bleed region I. cowl forward			
3.300–3.500	0.025	0.415	2.5
Bleed region II. centerbody forward			
3.546–3.644	0.125	0.415	0.5
Bleed region III. cowl throat			
3.846	0.125	0.415	0.5
3.928	0.125	0.415	0.5
Bleed region IV. centerbody throat			
3.751	0.125	0.415	0.5
3.784	0.125	0.415	0.5
3.816	0.125	0.415	0.5
3.897	0.125	0.415	0.5
3.979	0.125	0.415	0.5

Table 2 Supercritical bleed rates and plenum pressures.

	Experiment		CFD	
Bleed region	$W_{\text{bld-}i}/W_C$	p_{plenum}/p_{t0}	$W_{\text{bld-}i}/W_C$	p_{plenum}/p_{t0}
I. cowl forward	0.021	0.119	0.021	0.119
II. centerbody forward	0.018	0.150	0.019	0.173
III. cowl throat	0.008	0.105	0.008	0.263
IV. centerbody throat	0.024	0.188	0.024	0.252

Table 3 Bleed plenum exit areas.

Bleed region	$C_D A_{\text{exit}}/A_C$
I. cowl forward	0.041958
II. centerbody forward	0.024931
III. cowl throat	0.007067
IV. centerbody throat	0.022408

The product $C_D A_{\text{exit}}$ was calculated using the approach discussed above using the supercritical conditions of the CFD simulation. Table 3 lists the values of $C_D A_{\text{exit}}$ for each plenum. The exit area is normalized by the cowl lip capture area A_C. The values were used in the CFD simulations using the fixed-exit bleed model. At the supercritical condition, the fixed-exit bleed model and the constant-pressure bleed model produce the same flowfield. The values of $C_D A_{\text{exit}}$ were held constant for the inlet simulations as the engine-face backpressure was increased to examine the performance and operation of the inlet.

B. Flow Domain and Boundary Conditions

The axisymmetric shape of the inlet and flowfield allowed a planar, axisymmetric flow domain to be used for the CFD simulations. Figure 4 shows the outline of the flow domain along with the boundaries of the seven grid blocks.

The nose of the centerbody is located at axial coordinate $x/r_c = 0.0$ and radial coordinate $r/r_c = 0.0$. Because the inflow was supersonic, the forward portion of the inflow boundary could be located just slightly ahead of the nose. Another inflow boundary was placed at an angle to the inflow, but ahead of the conical shock emanating from the nose. The conical shock approached close to the cowl lip and exited through the external outflow boundary, which was located a distance of $0.6r_c$ downstream of the cowl lip. The cowl lip was located at coordinates $(x/r_c, r/r_c) = (2.33, 1.0)$. The flow boundary conditions were held fixed at the supersonic inflow boundary while an extrapolation boundary condition was applied for the supersonic outflow at the external outflow boundary. On the inlet surfaces, the flow boundary conditions imposed adiabatic, no-slip conditions. Within the bleed regions, the bleed boundary condition was imposed. The engine face was located at the axial coordinate $x/r_c = 5.375$. A constant-area extension and converging–diverging nozzle were attached to the engine face to reduce any potential boundary condition errors from affecting the measurement of total pressure at the engine face. The extension was a duct of length r_c. The converging–diverging nozzle accelerated the outflow to sonic conditions at the nozzle throat and then to supersonic conditions downstream of the throat. The outflow boundary condition was a supersonic extrapolation condition, which is nonreflecting and well behaved. The length of the nozzle is $1.6r_c$ with the throat at the middle. The outflow of the nozzle was at axial coordinate $x/r_c = 8.055$. The nozzle was also used to set the level of backpressure at the engine face. As the radius, and so the cross-sectional area, of the nozzle throat decreased, the backpressure increased. The throat radius was changed by replacing the CFD grid block for the nozzle. This computational procedure mimicked the reduction of the throat area of the mass-flow plug used to increase the backpressure in the wind-tunnel experiment.

C. Grid Resolution and Convergence

A planar, structured grid consisting of seven grid blocks containing H grids was generated for the flow domain. Figure 4 shows the outlines of the grid blocks. The number and distribution of grid lines within the grid blocks were based on several key grid spacings (distance between two adjacent grid points) that established the

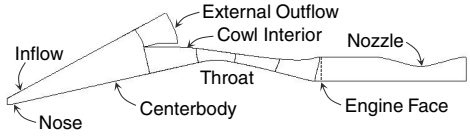

Fig. 4 Flow domain for the CFD simulations of the inlet.

resolution of the features of the flow. A key grid spacing was the spacing of the grid lines normal to the inlet surfaces. The grids were clustered near the inlet surfaces to resolve the gradients within the turbulent boundary layers. It was determined that a wall spacing of 0.0005 in. resulted in a nondimensional grid spacing of $0.5 < y^+ < 2.0$ throughout the inlet for the first grid line off of the inlet surfaces. Further, the grid was constrained to limit the rate of increase of grid spacing of adjacent grid lines away from the wall, which is known as grid stretching. A limit of 15% increase in the grid spacing between adjacent grid points is considered acceptable for RANS CFD simulations.

Another key grid spacing was the streamwise spacing of grid lines in the bleed regions and inlet throat. An additional constraint imposed for the bleed regions and inlet throat was that the grid lines should be approximately evenly-spaced in the streamwise direction. Further, between the cowl lip and throat, the quadrilateral cells should have an aspect ratio close to unity in the core inlet flow. These constraints provided a better grid for resolving the oblique shocks between the cowl lip and throat.

A grid-convergence study was performed to determine the proper value of the streamwise grid spacing in the bleed regions and throat. Two grids were generated: one with a throat spacing of 0.05 in. and one with a throat spacing of 0.075 in. For both grids, the other key grid spacing values were kept the same. This included the streamwise grid spacings at the nose (0.05 in.), cowl lip (0.02 in.), and engine face (0.1 in.). Based on these grid spacing values and grid constraints, the grids were generated by providing the adequate number of streamwise and cross-stream grid points. Two levels of coarser grids could be obtained from each grid by using grid sequencing in which the simulation was solved on every other grid line in each direction. With two grids and three levels of grid sequencing, the grid-convergence study involved six CFD simulations.

Each simulation was performed until iterative convergence. Iterative convergence was evaluated by examining the variations with iterations of the engine-face flow ratio W_2/W_C, average total pressure recovery p_{t2}/p_{t0}, average Mach number at the engine face M_2, and the bleed rates $W_{\text{bld-}i}/W_C$. The engine-face flow ratio, average total pressure recovery, and Mach number at the engine face were able to routinely converge over a sizable (thousands) number of iterations without change in the third decimal place (0.001). Similarly the bleed rates in percentage of the capture flow converged to the fourth decimal place (0.0001). Based on these findings, these properties were used to determine the iterative convergence of each CFD simulation.

Over the range of grids, the engine-face flow ratio, average Mach number, and total pressure recovery varied by less than 0.8% of the value on the finest grid. Between the two finest grids, these properties varied by less than 0.27%. Over the range of grids, the bleed rates for the individual bleed regions showed variations with a range of 0.21 to 0.39% of the inlet capture flow W_{bleed}/W_C. At the finest grids, the change in bleed rates varied from 0.11 to 0.35%. This change can be significant because the target bleed rates for the bleed regions ranged from 0.8 to 2.4%. These variations indicate that the bleed rates had the greatest impact on the grid resolution. The critical aspect for grid convergence seemed to be the resolution of the impinging oblique and normal shocks of the shock/boundary-layer interactions within the bleed regions. The bleed rate changed significantly based on where within the bleed region the shock impinged. Based on the results of the grid-convergence study, the finest grid with the streamwise throat spacing of 0.05 in. was used for the CFD simulations reported below. An uncertainty of the bleed rates is estimated to be between 0.11 and 0.35% of the reference captured flow rate. Given that the diameter of the bleed holes is 0.125 in., this suggested that one should use a grid spacing of 0.4 the diameter of the bleed hole ($0.4D$) or about two grid points for each bleed hole.

The planar grid about the cowl lip and throat of the inlet, respectively, are shown in Figs. 5 and 6. To clearly display the grid lines, the grids only show every other grid line in each direction. The grid contained 563 streamwise grid points from the cowl lip to the engine face. At the cowl lip, the grid consisted of 201 grid points between the centerbody and cowl lip. The grid stretching was less than 7% within the boundary layer away from the wall. This placed four to five grid points within a nondimensional spacing of $y^+ \leq 5$ next to the viscous surfaces.

D. Turbulence Modeling

The inlet flowfield is mostly turbulent, but some laminar flow was expected along the leading portions of the centerbody and cowl. The CFD simulations modeled laminar to turbulent transition by specifying the start and end location of a transition region. Within this region, the eddy viscosity ramped from its laminar value to its turbulent value. On the centerbody, the transition was specified to occur between axial coordinates $x/r_c = 2.45$ to 2.60. On the cowl, the transition was specified to occur between $x/r_c = 3.15$ to 3.25. These transition regions were determined by successive CFD simulations with various locations of the transition regions until boundary-layer profiles on forward locations on the centerbody and cowl matched within reason to those reported from the wind-tunnel experiment. This improved the similarity of the boundary-layer profiles entering the inlet between the experiment and CFD simulations.

Both the one-equation Spalart–Allmaras and two-equation Menter shear stress transport (SST) turbulent models were used to compute the turbulent eddy viscosity. For both models, the default settings of the Wind-US code were used. For the SST model, this included a compressibility dissipation correction. Both models produced only slightly different results. The difference between the total pressure recoveries was about 0.0050, or 0.58%. The difference between the

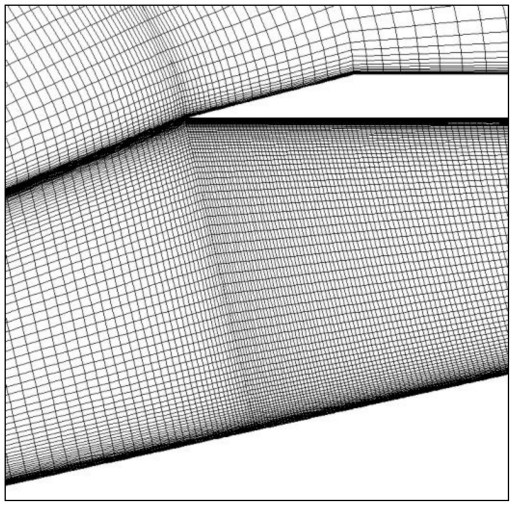

Fig. 5 Planar grid about the cowl lip (every other grid line is plotted).

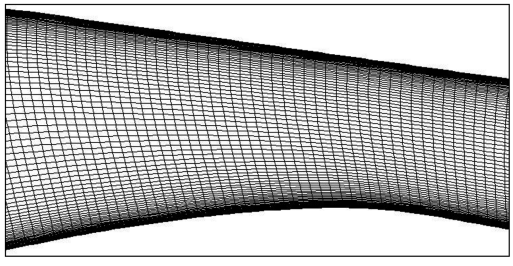

Fig. 6 Planar grid through the inlet throat (every other grid line is plotted).

engine-face flow ratios was 0.0033, or 0.35%. The difference between the total bleed flow ratios was 0.0039, or 5.5%. Although either model was acceptable, the SST model was chosen to produce the results shown in this paper.

E. CFD Flowfield Features

Some of the flow features of the flow between the cowl lip and throat can be seen in Fig. 7. The Mach number contours are plotted along with momentum vectors for the bleed at each of the grid points within the bleed regions. The discrete groupings of arrows for bleed region III and IV indicate the individual bleed rows.

The oblique shock from the cowl lip was reflected off of the centerbody. This reflected shock was reflected off the cowl at the end of bleed region I. The third reflected shock interacted with bleed region II and resulted in increased bleed flow downstream of the interaction. A weaker shock was reflected from the centerbody and several other weaker reflections are suggested before the terminal shock. The terminal shock is shown at the downstream edge of the last row in bleed region IV. For subsequent CFD simulations, the backpressure at the engine face was increased, which moved the terminal shock forward and caused greater interaction of the terminal shock with bleed regions III and IV and so created greater bleed rates for these two bleed regions. The flowfield ahead of the terminal shock, which included bleed regions I and II showed no change as the backpressure was increased.

F. Characteristic Cane Curves

The performance of the inlet was represented by the characteristic cane curves in which variation of the engine-face total pressure recovery (p_{t2}/p_{t0}) was plotted with respect to the variation of the total bleed flow ratio ($W_{\text{bld-}T}/W_C$) or the engine-face flow ratio (W_2/W_C). The cane aspect comes from the general shape of the curves. As the terminal shock interacts with the bleed regions in the throat, the increased bleed rates reduce the engine-face flow rate and the curve bends over. The part of the curve where the turning begins is referred to as the knee of the curve and is typically the preferred operating point for the inlet. Figure 8 shows the cane curves for the experiment along with error bars to show the level of uncertainty in the measurement of the total bleed flow ratio (±0.5%) and the engine-face flow ratio (±2.0%). At the higher engine-face flow ratios, the inlet operated in supercritical mode with the terminal shock downstream of all the bleed regions. The flow was supersonic over the bleed regions and the bleed rates and engine-face flows were constant. This formed the vertical portion of the canes. The variation in the vertical portion is due to variation in the engine-face static pressure or backpressure. As the backpressure increases, the terminal shock moves forward in the inlet to balance pressures and moves into regions of lower Mach number. This results is less total pressure loss through the shocks and so higher total pressure recovery at the engine face. As the backpressure was increased, the terminal shock moved forward and the total pressure recovery increased. As the terminal shock encountered bleed regions III and IV, the higher pressure behind the terminal shock forced more flow through the bleed holes and the engine-face flow decreased. This formed the knee portion of the cane curve. With further backpressure, the bleed and recovery increased while the engine-face flow decreased. At some level of backpressure, the throat bleeds are no longer able to contain the terminal shock and the shock moves forward of the throat bleed regions and the onset of inlet unstart has occurred. The data indicate

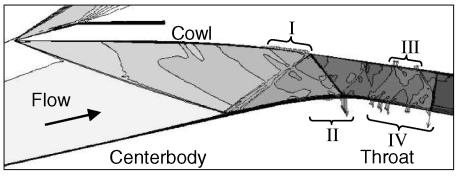

Fig. 7 Mach number contours and bleed momentum vectors in the inlet.

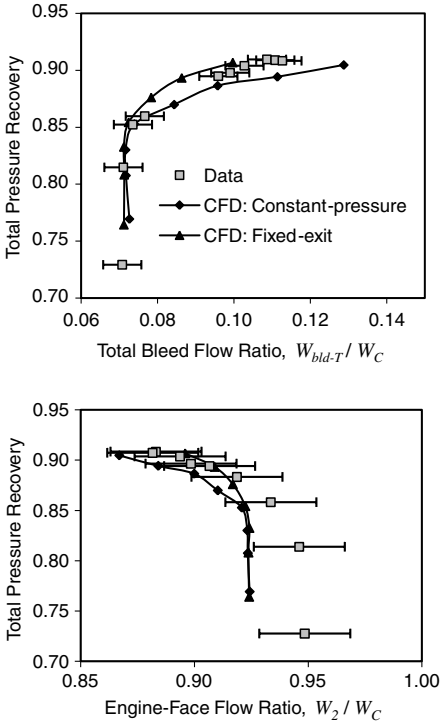

Fig. 8 Characteristic cane curves.

the onset of unstart occurred when the engine-face flow ratio went below 0.88. At this point, the terminal shock was pushed forward of bleed regions III and IV and the inlet experienced unstart. Figure 8 also shows the cane curve with respect to the total bleed flow ratio $W_{\text{bld-}T}/W_C$.

CFD simulations were performed to generate cane curves using both the constant-pressure and fixed-exit bleed models. The simulations started with the supercritical simulations discussed in preceding sections that were used to match the bleed rates with the experiment and evaluate the values of the plenum pressures for the constant-pressure bleed model and the $C_D A_{\text{exit}}$ for the fixed-exit bleed model. These bleed properties were held fixed as several simulations were performed with increased levels of backpressure to generate the cane curve using the fixed-exit bleed model. Figure 8 shows the cane curves for the CFD simulations using the constant-pressure and the fixed-exit bleed models.

The cane curves from the CFD simulations show good agreement with the data. The simulations seem to accurately capture the knee part of the curve. The plots of the total pressure recovery versus the engine-face flow ratio show that the CFD simulations indicated a lower engine-face flow ratio than the data; however, there is an inconsistency in the wind-tunnel data. At the supercritical condition, the data indicate a 0.07 bleed ratio and a 0.95 engine-face flow ratio; however, added together they should not exceed 1.00 of the captured flow. The data is likely showing the artifact of the 2% error in measuring mass flows. The cane curve with respect to the total bleed flow ratio reflects the matching of the bleed rates for the CFD simulations at the supercritical condition. The simulations with the constant-pressure bleed model were able to reach an engine-face flow ratio of 0.85 without unstart. No simulations were performed at higher backpressures. The simulations with the fixed-exit bleed model indicated the inlet would unstart when the engine-face flow ratio went below 0.89, which is close to the 0.88 indicated by the data. Thus, the fixed-exit bleed model provided a more realistic evaluation of the onset of inlet unstart than the constant-pressure bleed model.

The simulations with the fixed-exit bleed model show higher total pressure recoveries at the lower bleed rates than the simulations with the constant-pressure bleed model. One possible explanation for this is that the fixed-exit model allows the plenum pressure to increase beyond the level held constant by the constant-pressure model. This reduces the amount of bleed flow for the bleed region. This causes the

terminal shock to move further forward in the throat where the incoming Mach number, and so the total pressure losses are less.

G. Surface Static Pressures

The surface static pressures through the inlet provide an examination of the interactions of shock waves with the inlet surfaces and variations of inlet pressures through the bleed regions. The surface static pressures along the centerbody and cowl are plotted in Fig. 9. The axial coordinate was normalized by the cowl radius r_c. The surface static pressures were normalized by the reference static pressure p_0. The profile of the centerbody and cowl are shown by the solid lines, but the geometry is not to scale. The bleed regions are indicated by the thicker solid lines and circles in the plot. Note that bleed regions III and IV consist of individual rows of bleed holes and their locations are shown in Fig. 9 as the solid circles. The data represent a supercritical flow condition in which the terminal shock was downstream of the throat. The uncertainty in the measurement of the static pressures was reported in [28] as $\pm 0.2\,\%$, which is too small to be shown in Fig. 9. The pressures from the CFD simulation are from a simulation that used the constant-pressure bleed model. Because the flow shown in Fig. 9 is supercritical, the constant-pressure and fixed-exit bleed models produce the same flowfield ahead of the terminal shock.

The interaction of the cowl shock with the centerbody occurred between axial coordinates $x/r_c = 3.2$ and 3.4. Figure 9 shows that the CFD simulation initially captured the rise in static pressure of the interaction but further along indicates a higher static pressure than the data. The CFD simulation produced a small separation bubble at the interaction. Downstream of the interaction, the CFD simulation indicated a slight expansion that lowered the static pressures on the centerbody. An oblique shock was reflected from the centerbody and interacted with the cowl at an approximate axial coordinate of $x/r_c = 3.5$. This shock was reflected from the cowl and interacted with the centerbody at an approximate axial coordinate of $x/r_c =$ 3.6. For both interactions, the CFD simulation indicated a sharp rise in static pressure, whereas the data suggest a more gradual rise. The gradual rise may indicate a thicker boundary layer for the experiment than indicated by the CFD simulation.

Within the throat, the flowfield from the CFD simulation indicated a number of weak oblique shocks reflecting between the centerbody and cowl starting at an axial coordinate of $x/r_c = 3.6$ until the terminal shock, which is not shown in Fig. 9. The data indicate that static pressures on the centerbody gradually decrease through the throat, which indicated the expansion of the flow along the bleed region IV. The CFD simulation also indicated this expansion, but the static pressures show localized decreases in static pressure over the individual parts of bleed region IV. On the cowl, there was less expansion, which was likely due to bleed region III being smaller. The CFD simulation indicated the local decreases in static pressure for the boundary grid points in the bleed region.

H. Bleed Rates

The bleed rates for bleed regions III and IV increased as the backpressure was increased at the engine face and the terminal shock was pushed upstream into the throat and the bleed regions. Figure 10 plots the increase of the bleed flow ratios for bleed regions III and IV with respect to the total bleed flow ratio for both the wind-tunnel data and the CFD simulations using both the fixed-exit and constant-pressure bleed models. The bleed flows in bleed regions I and II did not change with increased levels of backpressure because those regions were ahead of the terminal shock. The bleed flow rates start with the supercritical bleed rates. Because the inputs for the bleed models were adjusted to match these bleed rates, the bleed rates from the CFD simulations match those of the data. As the total bleed rate increases, the bleed rates of regions III and IV from the CFD simulation using the fixed-exit bleed model increase in a similar manner as the wind-tunnel data. This suggests that the fixed-exit bleed model can accurately indicate the change in the bleed flows of the individual bleed regions with increased levels of backpressure. The plots for the fixed-exit CFD simulations stop at a total bleed flow ratio of 0.10, which indicates the last simulation before the onset of inlet unstart. The wind-tunnel data indicate inlet unstart occurred after a total bleed flow ratio of 0.11. The plots for the constant-pressure CFD simulations are shown in Fig. 10. Up until a total bleed flow ratio of approximately 0.095, the bleed rate of region III remains almost constant for the constant-pressure CFD simulation, whereas the bleed rate of region IV increases. This occurs because region IV is further downstream of region III and starts bleeding at a greater rate and delays the movement of the terminal shock into region III. Above a total bleed flow ratio of 0.095, the bleed rates of regions both III and IV continue to increase to a total bleed flow ratio of approximately 0.13 without the onset of inlet unstart. This demonstrates the increased stability margin against inlet unstart provided by a constant-pressure bleed system, albeit at the expense of greater bleed rates.

I. Bleed Plenum Pressures

The ability to simulate the plenum pressure is of importance in inlet design because it allows estimation of the bleed drag. A higher plenum pressure usually results in lower bleed drag. For a bleed plenum with a fixed-exit area, the plenum pressure will increase as the level of backpressure is increased and the terminal shock moves forward across the bleed region. Figure 11 shows the bleed plenum pressurizations with respect to the total bleed flow ratio for bleed regions III and IV for the experiment and the CFD simulations with the fixed-exit and constant-pressure bleed models. Because bleed regions I and II are forward of the terminal shock, they experience no pressurization and are not shown. As indicated in Table 2, the pressures from the supercritical simulations are higher than those indicated from the data. This is reflected in the higher pressures for the supercritical condition. The slope of the variation for bleed region IV is similar to the wind-tunnel data, although at an offset of a higher bleed plenum pressure ratio. The pressure for bleed region III does not change at first, which indicates that the terminal shock has not yet interacted with region III. Above a total bleed flow ratio of 0.08, the plenum pressure of region III increases at a greater rate than

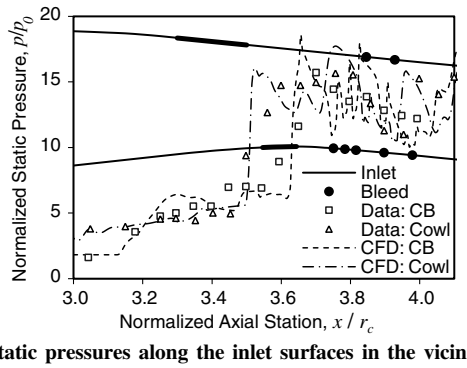

Fig. 9 Static pressures along the inlet surfaces in the vicinity of the bleed regions.

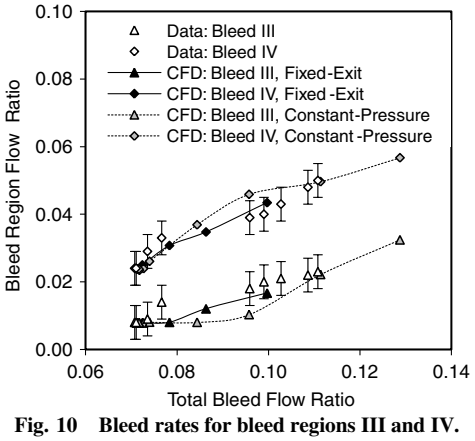

Fig. 10 Bleed rates for bleed regions III and IV.

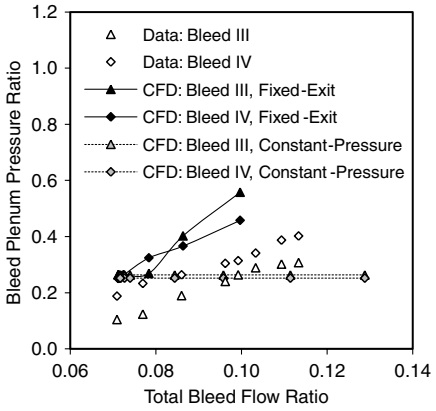

Fig. 11 Bleed plenum static pressure ratios for bleed regions III and IV.

the wind-tunnel data. The reason for these differences in the plenum pressures is not fully understood. The differences are likely due to a combination of the complexity of the flow, uncertainties in the bleed model, and uncertainties in the turbulence model. Further, there are uncertainties in the data. For example, the report did not clearly indicate where the plenum pressures were measured. It was assumed that static pressure taps existed within the plenums. However, the schematic of the tunnel model shows total pressure probes in the exit duct for bleed region IV.

IV. Conclusions

A model for porous bleed systems with fixed-exit plenums for supersonic inlets has been described and CFD simulations have demonstrated the behavior of the model. The model was implemented into the Wind-US CFD code and was used to simulate steady flow in a Mach 3, axisymmetric, mixed-compression inlet. The model was able to simulate the spatial variation of bleed rates along the bleed regions as shocks interacted with the bleed regions. The CFD simulation results for the total pressure recovery and bleed rates compared well with wind-tunnel data. The fixed-exit model was able to calculate the plenum pressure rather than require it to be specified; however, the model indicated higher plenum pressures in the throat than those of the wind-tunnel data. The fixed-exit model was able to simulate the onset of inlet unstart due to the increased level of backpressure for bleed systems with fixed bleed plenum exit areas. The study has provided useful information on the modeling of porous bleed regions for CFD simulation of supersonic inlets.

Yet, challenges continue to exist with regard to porous bleed modeling. Among the challenges includes the improvement of the empirical basis for the sonic flow coefficient Q_{sonic} to account for the various factors that affect the bleed rate, such as hole geometry, approach boundary layer, and core inlet-flow nonuniformity. Further, an improvement may be to correlate Q_{sonic} with flow properties on the surface near the bleed hole, such as surface static pressure, rather than properties at the edge of the boundary layer. Another challenge is the modeling of recirculation in the bleed region in which a portion of the bleed region may be injecting flow into the core inlet flow. This may occur when the plenum static pressure is close to the local inlet pressure and a shock is interacting with the bleed region. Downstream of the shock, the increased local pressure results in bleeding while ahead of the shock interaction point, the lower core pressures results in injection. Another challenge is the modeling of the tangential component of velocity and the production of turbulence in the bleed region. This may be significant when considering the effect of the bleed on the boundary-layer profiles downstream of the bleed region. One objective of bleed is to improve the boundary-layer profile. Related to this is the concept of bleed roughness in which the presence of the bleed holes and bleed flow adds surface roughness that can affect the boundary-layer development. The turbulence models could likely be improved by modeling the roughness and change in velocity components within the bleed regions. A further challenge of bleed modeling is to recognize the individual bleed holes rather than assuming a continuous porous bleed surface. This would require greater resolution of the bleed region and the individual bleed holes.

Acknowledgments

The authors wish to thank the sponsors of this work, including the NASA Glenn Research Center, Fundamental Aeronautics Program, Hypersonics Project (James L. Pittman, Principal Investigator) and the Office of Naval Research (ONR) (Joseph Doychak, Program Manager, Code 351). Funding by ONR for this effort used Space Act Agreement NAS3-598 between NASA Glenn Research Center at Lewis Field and NAVAIR Propulsion and Power Engineering Department (William Voorhees, Chief Technology Officer). The authors also wish to thank Charles Trefny of the NASA Glenn Research Center at Lewis Field for beneficial technical discussions.

References

[1] Seddon, J., and Goldsmith, E. L., *Intake Aerodynamics*, AIAA Education Series, AIAA, New York, 1985.

[2] Tjonneland, E., "The Design, Development, and Testing of a Supersonic Transport Intake System," AGARD CP-91-71, Dec. 1971, pp. 18-1–18-17.

[3] Syberg, J., and Hickox, T. E., "Design of a Bleed System for a Mach 3.5 Inlet," NASA CR-2187, Jan. 1973.

[4] Fukuda, M. K., Hingst, W. R., and Reshotko, E., "Control of Shock Wave-Boundary Layer Interactions by Bleed in Supersonic Mixed Compression Inlets," NASA CR-2595, Aug. 1975.

[5] Delery, J., "Shock-Wave/Turbulent Boundary-Layer Interaction and Its Control," *Progress in Aerospace Sciences*, Vol. 22, No. 4, June 1985, pp. 209–280.
doi:10.1016/0376-0421(85)90001-6

[6] Hamed, A., and Shang, J., "Survey of Validation Data Base for Shock Wave Boundary Layer Interactions in Supersonic Inlets," *Journal of Propulsion and Power*, Vol. 7, No. 4, July 1991, pp. 617–625; also AIAA Paper 1989-2939, July 1989.
doi:10.2514/3.23370

[7] Sanders, B. W., and Cubbison, R. W., "Effect of Bleed-System Back Pressure and Porous Area on the Performance of an Axisymmetric Mixed Compression Inlet at Mach 2.50," NASA TM X-1710, Dec. 1968.

[8] Sanders, B. W., and Mitchell, G. A., "Increasing the Stable Operating Range of a Mach 2.5 Inlet," AIAA Paper 1970-0686, June 1970; also NASA TM X-52799, June 1970.

[9] Mitchell, G. A., and Sanders, B. W., "Poppet Valve Control of a Throat Stability Bypass to Increase the Stable Airflow Range of a Mach 2.5 Inlet with 60-Percent Internal Contraction," NASA TM X-3297, Oct. 1975.

[10] Chyu, W. J., Kawamura, T., and Bencze, D. P., "Navier–Stokes Solutions for Mixed-Compression Axisymmetric Inlet Flow with Terminal Shock," *Journal of Propulsion and Power*, Vol. 5, No. 1, 1989, pp. 4–5; also AIAA Paper 1987-0160.
doi:10.2514/3.23106

[11] Reddy, D. R., and Weir, L. J., "Three-Dimensional Viscous Analysis of a Mach 5 Inlet and Comparison with Experimental Data," *Journal of Propulsion and Power*, Vol. 8, No. 2, 1992, pp. 432–440; also AIAA Paper 1990-600, Jan. 1990.
doi:10.2514/3.23496

[12] Fujimoto, A., Niwa, N., and Sawada, K., "Numerical Investigation of Supersonic Inlet with Realistic Bleed and Bypass System," *Journal of Propulsion and Power*, Vol. 8, No. 4, 1992, pp. 857–861; also AIAA Paper 1991-127, Jan. 1991.
doi:10.2514/3.23560

[13] Mayer, D. W., and Paynter, G. C., "Boundary Conditions for Unsteady Supersonic Inlet Analyses," *AIAA Journal*, Vol. 32, No. 6, June 1994, pp. 1200–1206.
doi:10.2514/3.12120

[14] Mayer, D. W., and Paynter, G. C., "Prediction of Supersonic Inlet Unstart Caused by Freestream Disturbances," *AIAA Journal*, Vol. 33, No. 2, Feb. 1995, pp. 266–275; also AIAA Paper 1994-580, Jan. 1994.
doi:10.2514/3.12418

[15] Slater, J. W., Davis, D. O., Sanders, B. W., and Weir, L. J., "Role of CFD in the Aerodynamic Design and Analysis of the Parametric Inlet," International Symposium on Air Breathing Engines Paper 2005-1168, Sept. 2005.

[16] Hamed, A., and Lehnig, T., "Investigation of Oblique Shock/Boundary

Layer/Bleed Interaction," *Journal of Propulsion and Power*, Vol. 8, No. 2, 1992, pp. 418–424; also AIAA Paper 1990-1928, July 1990. doi:10.2514/3.23494

[17] Shih, T. I.-P., Rimlinger, M. J., and Chyu, W. J., "Three-Dimensional Shock-Wave/Boundary-Layer Interaction with Bleed," *AIAA Journal*, Vol. 31, No. 10, Oct. 1993, pp. 1819–1826. doi:10.2514/3.11854

[18] Rimlinger, M. J., Shih, T. I.-P., and Chyu, W. J., "Shock-Wave/Boundary-Layer Interactions with Bleed Through Rows of Holes," *Journal of Propulsion and Power*, Vol. 12, No. 2, 1996, pp. 217–224; also AIAA Paper 1994-313, Jan. 1994. doi:10.2514/3.24016

[19] Hamed, A., Yeuan, J. J., and Jun, Y. D., "Flow Characteristics in Boundary-Layer Bleed Slots with Plenum," *Journal of Propulsion and Power*, Vol. 12, No. 2, 1996, pp. 231–226; also AIAA Paper 1995-33, Jan. 1995. doi: 10.2514/3.24018

[20] Chyu, W. J., Howe, G. W., and Shih, T. I.-P., "Bleed Boundary Conditions for Numerically Simulated Mixed-Compression Supersonic Inlet Flows," *Journal of Propulsion and Power*, Vol. 8, No. 4, 1992, pp. 862–868. doi:10.2514/3.23561

[21] Paynter, G. C., Treiber, D. A., and Kneeling, W. D., "Modeling Supersonic Inlet Boundary Layer Bleed Roughness," *Journal of Propulsion and Power*, Vol. 9, No. 4, 1993, pp. 622–627; also AIAA Paper 1992-269, Jan. 1992. doi:10.2514/3.23666

[22] Harloff, G. J., and Smith, G. E., "Supersonic-Inlet Boundary-Layer Bleed Flow," *AIAA Journal*, Vol. 34, No. 4, 1996, pp. 778–785; also AIAA Paper 1995-0038, 1995. doi:10.2514/3.13140

[23] Dambara, S., Yamamoto, M., and Honami, S., "Modeling of Boundary Conditions for Turbulent Boundary Layer Bleed," AIAA Paper 1998-0926, Jan. 1998.

[24] Benson, D. B., Shih, T. I.-P., Davis, D. O., and Willis, B. P., "Boundary Conditions for CFD Simulations of Supersonic Boundary-Layer Through Discrete Holes," AIAA Paper 2000-0888, Jan. 2000.

[25] Frink, N., Bonhaus, D., Vatsa, V., Bauer, S., and Tinetti, A., "A Boundary Condition for Simulation of Flow Over Porous Surfaces," AIAA Paper 2001-2412, June 2001.

[26] Akatsuka, J., Watanabe, Y., Murakami, A., and Honami, S., "Porous Bleed Model for Boundary Conditions," AIAA Paper 2006-3682, June 2006.

[27] Mani, M., Cary, A., and Ramakrishnan, S., "A Structured and Hybrid-Unstructured Grid Euler and Navier–Stokes Solver for General Geometry," AIAA Paper 2004-0524, Jan. 2004.

[28] Sorensen, N. E., and Smeltzer, D. B., "Investigation of a Large-Scale Mixed-Compression Axisymmetric Inlet System Capable of High Performance at Mach Numbers 0.6 to 3.0," NASA TM X-1507, Feb. 1968.

[29] McLafferty, G., and Ranard, E., "Pressure Losses and Flow Coefficients of Slanted Perforations Discharging from Within a Simulated Supersonic Inlet," United Aircraft Corp., Research Dept., Rept. R-0920-1, East Hartford, CT, 1958.

[30] Willis, B. P., Davis, D. O., and Hingst, W. R., "Flow Coefficient Behavior for Boundary Layer Bleed Holes and Slots," AIAA Paper 1995-0031, Jan. 1995; also NASA TM-106846, Dec. 1994.

F. Liu
Associate Editor